

RESEARCH ARTICLE

10.1002/2016JD024933

Key Points:

- The first 1 km resolution AVHRR BRDF and albedo data set from 1990 to 2014 for Europe is presented
- Analysis of shortwave albedo anomalies is insufficient as albedo anomalies in VIS and NIR are mostly contrasting
- Climate variation and vegetation response are reflected in spectrally distinct spatiotemporal albedo patterns

Correspondence to:

M. Sütterlin,
melanie.suetterlin@giub.unibe.ch

Citation:

Sütterlin, M., R. Stöckli, C. B. Schaaf, and S. Wunderle (2016), Albedo climatology for European land surfaces retrieved from AVHRR data (1990–2014) and its spatial and temporal analysis from green-up to vegetation senescence, *J. Geophys. Res. Atmos.*, 121, 8156–8171, doi:10.1002/2016JD024933.

Received 11 FEB 2016

Accepted 12 JUN 2016

Accepted article online 15 JUN 2016

Published online 18 JUL 2016

Albedo climatology for European land surfaces retrieved from AVHRR data (1990–2014) and its spatial and temporal analysis from green-up to vegetation senescence

M. Sütterlin¹, R. Stöckli², C. B. Schaaf^{3,4}, and S. Wunderle^{1,5}
¹Institute of Geography, University of Bern, Bern, Switzerland, ²Federal Office of Meteorology and Climatology, MeteoSwiss, Zürich, Switzerland, ³School for the Environment, University of Massachusetts Boston, Boston, Massachusetts, USA,

⁴Department of Earth and Environment, Boston University, Boston, Massachusetts, USA, ⁵Oeschger Centre for Climate Change Research, University of Bern, Bern, Switzerland

Abstract Satellite-based, long-term records of surface albedo characterization that accurately capture spatial and temporal patterns are essential to develop climate models and to monitor the impact of land use changes on the terrestrial energy and water balance. This study presents the first Bidirectional Reflectance Distribution Function (BRDF) and albedo data set derived from the Advanced Very High Resolution Radiometer (AVHRR) Local Area Coverage reflectance data acquired on board National Oceanic and Atmospheric Administration and Meteorological Operational platforms from 1990 to 2014 over Europe. The objectives of this paper are to describe the data set's surface albedo climatology and anomalies in the visible, near-infrared, and shortwave broadbands for the growing season months of May to September in order to facilitate utilization of the data by the climate modeling communities. The results demonstrate that the AVHRR BRDF and albedo data have temporal and spatial patterns that are appropriate for the underlying predominant land cover type and accurately reflect the associated climate variation. Visible and near-infrared broadband albedo anomalies are found to be contrasting in most years, and their spatial distributions depict responses of vegetation to climate events (e.g., heat waves). Visible albedo of crops and near-infrared albedo of pastures show a higher interannual variation than respective albedos of other snow-free land covers, while the interannual standard deviations are found to be lower than 0.015. Our findings indicate the importance of taking into account the spectrally distinct variability of surface albedo when analyzing its complex spatiotemporal dynamics in climate-related research.

1. Introduction

Characterizing spatial heterogeneity and temporal variation of surface albedo is of great importance to monitor land cover change and to determine energy exchange between ground and atmosphere. Land surface albedo, which quantifies the reflectivity of the land surface and is listed as an Essential Climate Variable [Pinty *et al.*, 2008; Schaaf *et al.*, 2009; *Global Climate Observing System*, 2011], is highly variable as it is influenced by many factors, including vegetation, snow coverage, soil moisture, and solar illumination. The resulting spatial and temporal variations are governed by both natural processes (e.g., phenological cycles of vegetation, snowfall, and change in solar position) and human activities (e.g., harvesting, deforestation, reforestation, and shifting cultivation) and also indicate environmental vulnerability [*Global Climate Observing System*, 2004]. Long-term records of surface albedo therefore are helpful to foster the understanding of global and regional land surface processes and are accordingly required for climate, hydrological, and biogeochemical modeling and weather forecasting [Schaaf *et al.*, 2009].

Traditionally, climate models have relied on a global land cover map or a grid box of land cover types to deduce the land surface albedo. The surface albedos prescribed to these land cover types have been primarily based on a set of compiled field measurements of albedo from different land cover types or remotely sensed climatologies with coarse spatial resolution, such as those derived from Earth Radiation Budget Experiment observations [Li and Garand, 1994]. While field measurements support the local and regional characterization of surface albedo, remote sensing offers the only effective method for measuring and monitoring the heterogeneity of albedo and its directional signature (related to the anisotropic reflectance properties of the land surface) on regional and global scales. Further, remote sensing is able to provide consistent estimates of land surface albedo at regular temporal intervals. However, cloud contamination, atmospheric correction, directional-hemispherical integration, and spectral interpolation (narrowband to broadband conversion) remain main sources of

uncertainty in the retrieval of surface albedo from remotely sensed data. Therefore, appropriate preprocessing is essential in order to accurately derive albedo from satellite imagery [Sütterlin *et al.*, 2015]. This applies in particular to imagery from older sensors, such as the Advanced Very High Resolution Radiometer (AVHRR), which holds great potential for the retrieval of long-term records of surface albedo, but also implies additional uncertainties, concerning, for example, calibration [Rao, 1987; Heidinger *et al.*, 2010] and orbital drift [Price, 1991].

When improving climate models, satellite observations of the land surface have become crucial in many respects: to define the initial state, to quantify changes in different types of forcing, to evaluate the accuracy of model simulations, and to help parameterize processes [Pitman, 2003; Widlowski *et al.*, 2011]. In line with climate model developments during recent decades, temporally resolved albedo parameterizations have been implemented, and the requirements for albedo have become more specific regarding the time and location of the application [Lawrence and Chase, 2007; Widlowski *et al.*, 2011; Loew *et al.*, 2014]. Thereby, when evaluating the accuracy of formulations in Land Surface Schemes, spatially explicit descriptions of the directional nature of land cover types and the directional scattering of the incident solar radiation have gained on interest [Widlowski *et al.*, 2011]. For instance, Moderate Resolution Imaging Spectroradiometer (MODIS) albedo data, which take the directional nature of the reflected radiation into account by integrating the Bidirectional Reflectance Distribution Function (BRDF) [Nicodemus *et al.*, 1977; Wanner *et al.*, 1995], now widely serve as reference data set for evaluating results from climate models. MODIS black-sky (directional-hemispherical) and white-sky (bihemispherical) albedo quantities are provided every 8 days for three broadbands and seven spectral bands spanning the visible to the near-infrared and midinfrared ranges [Lucht *et al.*, 2000; Schaaf *et al.*, 2002, 2011]. Actual (blue-sky) albedo can be calculated by combining these two quantities as a function of the fraction of diffuse skylight [Lewis and Barnsley, 1994; Román *et al.*, 2010]. For example, Boisier *et al.* [2013] use MODIS shortwave white-sky albedo to estimate albedo changes and evaluate land use induced albedo changes simulated by various climate models participating in the Land Use and Climate: IDentification of robust impacts inter-comparison (LUCID) project. They find that although the intermodel mean simulated albedo change is consistent with the MODIS-based reconstruction, individual models show significant differences. Zhang *et al.* [2010] compare shortwave albedo results from 21 General Circulation Models (GCMs) collected by the Program for Climate Model Diagnosis and Intercomparison (PCMDI) with MODIS shortwave albedo data for 2000 to 2008 and show that differences between remotely sensed and GCM-simulated annual averages of global albedo can be as large as 0.06, while simulated albedos are mostly lower. Agreements between MODIS albedo and albedo simulated by climate models, furthermore, are revealed to depend on the region, surface type, and season. The difference between the albedos is generally higher for winter than for summer, while the spatial distribution of the difference is mainly governed by land surface heterogeneity and topography [Roesch *et al.*, 2004; Wang *et al.*, 2006]. Accordingly, high-quality surface albedo characterization that accurately captures spatial and temporal features continues to be a high priority for modeling efforts [Gao *et al.*, 2005]. Moreover, long-term albedo characterization comparable to the MODIS albedo data is needed to allow for similar and extended long-term comparisons, in order to contribute to the development of climate models and to improve their reliability.

This study presents and explores a satellite-based BRDF/albedo data set retrieved from Local Area Coverage (LAC) reflectance data of the AVHRR for the months May to September approximately capturing vegetation green-up to senescence in Europe. For the retrieval, an AVHRR-adapted MODIS BRDF and albedo methodology is employed on AVHRR imagery gathered on board National Oceanic and Atmospheric Administration (NOAA) and Meteorological Operational (MetOp) satellites from 1990 to 2014. The performance of this AVHRR methodology and the quality of the retrievals have been assessed previously, and first validations of a 13 year data set have been conducted [Sütterlin *et al.*, 2015]. This study extends the AVHRR BRDF/albedo data set to 25 years and examines spectral and spatiotemporal patterns across Europe and intraseasonal and interannual variations for different land cover types. Prevalent and striking spatial and temporal patterns in albedo variability are identified, and possible reasons for the variability are investigated. For this purpose, the study evaluates spatial albedo anomalies in different spectral ranges, compares them to anomalies of climate variables, and, finally, considers differences in albedo response between the major land cover types.

2. Data

2.1. AVHRR BRDF and Albedo Data Set

The AVHRR BRDF/albedo data set is retrieved from the comprehensive European LAC AVHRR data archive of the University of Bern described in Hüsler *et al.* [2011]. BRDF model parameters, black-sky and white-sky

albedos, and Nadir BRDF-Adjusted surface Reflectance (NBAR) in Lambert Conformal Conical (LCC) projection with a spatial resolution of 1 km and extensive quality information are included. The three BRDF model parameters (f_{iso} , f_{vol} , f_{geo}) are provided for the first two spectral bands of the AVHRR sensor centered around 0.6 μm and 0.8 μm , respectively, and for three broadbands (visible, near-infrared, and shortwave). The intrinsic black-sky albedo quantity (directional-hemispherical reflectance) at local solar noon and white-sky albedo quantity (bihemispherical reflectance) are supplied for the respective two spectral bands and three broadbands. Both quantities are derived by integrating the BRDF calculated from the parameters (f_{iso} , f_{vol} , f_{geo}). The NBAR data provide spectral reflectance adjusted to the sensor appearing nadir to the target pixel while the Sun is positioned to the mean solar zenith angle of the angular sampling period of 16 days. In addition, each AVHRR BRDF, NBAR, and albedo retrieval is accompanied by quality information based on per-pixel quality assurance fields indicating whether the retrieval was successful and whether the result is of the high-quality or should be used with caution.

The retrieval of the AVHRR BRDF data relies on the inversion of the semiempirical Ross-Thick/Li-Sparse-Reciprocal (RTLSR) kernel-driven model corresponding to the MODIS BRDF/albedo methodology [Schaaf *et al.*, 2002, 2011; S  tterlin *et al.*, 2015]. Sequential multiangle, cloud-free, and atmospherically corrected surface reflectance observations built up over a moving input window of 16 days are employed to calculate the RTLSR BRDF model parameters that describe an estimate of the BRDF shape. Differences to the MODIS BRDF/albedo processing scheme are mainly related to the quantification of uncertainties in the atmospherically corrected input observations prior to the actual inversion and the preprocessing of the satellite data. In addition, the AVHRR backup database allows reliable BRDF retrievals with the magnitude inversion technique which extensively supplement the full retrievals if the number of observations or the variability in angular sampling is insufficient to accomplish a retrieval with the main algorithm. The backup algorithm that uses the parameters from the database as a first BRDF shape approximation and fits this predetermined shape to the magnitude of any available observations acquired within the 16 day window most often performed quite well under normal conditions. In most circumstances, differences in accuracy between full inversion retrievals and backup magnitude inversion retrievals were found to be minor [Jin *et al.*, 2003; Salomon *et al.*, 2006; Liu *et al.*, 2009; Wang *et al.*, 2010]. However, the backup retrievals are flagged and should be considered a reduced quality result. A detailed description of the AVHRR BRDF and albedo processing scheme, comprehensive quality assessment of the AVHRR BRDF/albedo data, and validation of albedo retrievals is given in S  tterlin *et al.* [2015]. The AVHRR BRDF and albedo retrievals were found to be of high quality across most of Europe and allow the accurate description of the in situ surface reflectance, with an overall absolute accuracy primarily within 0.05 throughout the complete seasonal cycle (with a minimum bias at the peak of the growing season).

2.2. Land Cover Classification and Gridded Climate Data Sets

Variability in albedo climatology for different types of land cover is considered based on the Coordinate Information on the Environment (CORINE) Land cover Classification (CLC). The CLC nomenclature includes 44 land cover classes that are grouped into five main categories referred to as artificial surfaces, agricultural areas, forest and seminatural areas, wetlands, and water bodies [Heymann *et al.*, 1994]. CLC maps for the reference years 1990, 2000, and 2006 are provided by the European Environmental Agency (EEA). The raster version of these CLC maps with a resolution of 100 \times 100 m was used to compile a multiyear stable land cover map for the investigated European subset (Figure 1) by aggregating pixels with consistent classification in all three reference years.

Independent data sets from the European Centre for Medium-Range Weather Forecasts (ECMWF) interim Reanalysis (ERA-Interim) [Dee *et al.*, 2011] and from the Global Precipitation Climatology Centre (GPCC) [Rudolf and Schneider, 2005] operated by the German National Meteorological Service (<http://www.dwd.de>) are included to consider climate variables in the context of spatial variability in annual anomalies of monthly averages. The monthly means of mean daily 2 m air temperature organized on a regular grid at 0.75 $^{\circ}$ \times 0.75 $^{\circ}$ spatial resolution from the ERA-Interim Reanalysis data and gridded monthly precipitation data at 1 $^{\circ}$ spatial resolution from the GPCC monitoring product were used to construct monthly air temperature and monthly precipitation anomalies, respectively.

These climate data sets and the CORINE data were resampled to match the LCC projection, and the AVHRR-based water mask was applied to screen the nonland pixels in order to consistently prevent water pixels from corrupting the land surface analysis.



Figure 1. Coordinate Information on the Environment (CORINE) Land Cover map covering the investigated European subset assembled by compiling consistent land cover pixels from CLC90, CLC00, and CLC06.

3. Methods

3.1. AVHRR BRDF/Albedo Processing

Time series of AVHRR BRDF/albedo data from 1990 to 2014 are generated by retrieving the BRDF every 8 days with a 16 day moving window. The 16 days are weighted equally, and the center of the moving window is associated with the date of each retrieval, which corresponds to the MODIS BRDF/albedo methodology applied for the MCD43A V005 product. With this 8 day overlapping procedure, four retrievals are provided for each investigated month (May, June, July, August, and September). The backup database consisting of seasonal BRDF weighting parameters is adjusted for each year by using the surrounding 10 years' worth of high-quality full model retrievals to estimate a first-guess approximation of the underlying reflectance anisotropy.

The number of observations utilized from different platforms is displayed per month in Figure 2. The acquisition period lasts from 23 April to 7 October during nonleap years and from 22 April to 6 October during leap years, respectively, while the first retrieval for May employs the observations from the 16 day period starting at the end of April, and the last retrieval for September employs the observations from the 16 day period reaching the beginning of October. Satellite-based radiometric measurements originating from AVHRR/2 instruments on board NOAA 9, 11, 12, and 14 and from AVHRR/3 instruments carried on board NOAA 15, 16, 17, 18, and 19 and MetOp-A and MetOp-B are included. Data acquired at different times of the day by several simultaneously operating satellites provide high variability in angular sampling, which is beneficial for the BRDF correction [Sütterlin *et al.*, 2015]. From 2003 to 2011, the AVHRR sensor reaches a maximum of two to three overpasses per day resulting in numerous observations with different combinations of viewing and solar angle. However, the number of orbiting satellites varies and, consequently, the number of observations and the variability in angular sampling are not equally distributed. Thus, in this time series application, the BRDF retrievals for the earlier years rely more frequently on the backup algorithm as the number of observations or the variability in angular sampling may be insufficient for a full model BRDF retrieval. Within the investigated time period from May to September, for example, 62.5% of the land surface albedos for 1990 are backup retrievals, 32% are full model retrievals, and 5.5% are fill values (no retrievals), whereas for 2014, 93.5% of the albedos are full model retrievals.

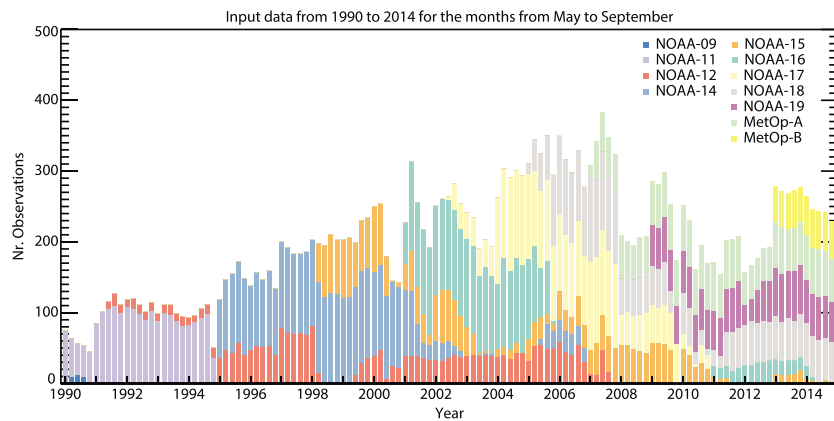


Figure 2. Monthly number of input observations utilized from different satellites within four 16 day retrieval periods for May (23 April to 1 June), June (25 May to 3 July), July (26 June to 4 August), August (28 July to 5 September), and September (29 August to 7 October) from 1990 to 2014.

Monthly albedo averages were derived by calculating the median for pixels with either full or magnitude retrievals, while a fill value was assigned to pixels if any of the 16 day acquisition periods within a month did not have at least a backup magnitude inversion. Furthermore, monthly albedo anomalies ($\Delta\alpha(y, m)$) were computed by calculating the difference between the monthly albedo average in a given year ($\alpha(y, m)$) and the mean monthly albedo average of all years of the same month ($\bar{\alpha}(m)$):

$$\Delta\alpha(y, m) = \alpha(y, m) - \bar{\alpha}(m) \quad (\text{Eq. 1})$$

The monthly averages and the monthly albedo anomalies were calculated for black-sky and white-sky albedos in the visible broadband, near-infrared broadband, and total shortwave broadband. In this study, the focus is mainly on white-sky albedo since the results for black-sky albedo show similar patterns and because white-sky albedo is an appropriate approximation of the daily means of surface albedo and comparable to that simulated in climate models [Boisier *et al.*, 2013]. Moreover, regarding the present study's investigation of variations between the albedo of different land cover types, there is only minor impact, since the differences between white-sky and black-sky albedos are mainly induced by variations in the solar zenith angle and not particularly determined by the type of vegetation [Boisier *et al.*, 2013].

3.2. Classification Scheme to Differentiate Albedo Climatologies for Major Land Cover Types

The investigation of the albedo climatology for different land cover types is expressed in terms of subgrouping of the 44 CORINE land cover classes. Together, the selected subgroups constitute around 83% of the investigated European subset, while the "non-irrigated arable land" class with around 27% of the land pixels represents most of the included land area (Table 1). The arable land subgroup is reduced to the class "non-irrigated arable land" while the classes "permanently irrigated land" and "rice fields" are excluded. Following the land use categories equivalence study considered in the context of surface parameters by Pineda *et al.* [2004], the subgroups "permanent crops" (vineyards, fruit trees and berry plantations, and olive groves) and "heterogeneous agricultural areas" are combined into a single group referred to as "crops/wood mosaic." Scrub and/or herbaceous vegetation associations are separated into a "natural grassland" subgroup and a "mix shrubland/grassland" subgroup. The forest classes "broad-leaved," "coniferous," and "mixed" and the "pastures" subgroup are reported separately. Finally, the classes "beaches, dunes, sands," "bare rocks," "sparsely vegetated areas," and "burnt areas" are grouped as "barren and sparsely vegetated areas." These subgroups were collocated with the AVHRR BRDF/albedo data by assigning each AVHRR pixel one of these land cover groups when more than 75% of the 1×1 km area is covered by a given subgroup. The resulting predominantly pure land cover pixels are used to differentiate the albedo between the subgroups.

4. Results and Discussion

4.1. Albedo Climatology for the Months May to September for Europe (1990 to 2014)

Long-term means and annual anomalies of monthly shortwave, near-infrared, and visible AVHRR black-sky and white-sky broadband albedo averages for the land surface of the European subset from 1990 to 2014

Table 1. Total Area and Percentage of Land Area Pixels of Land Cover Type Subgroups Within the Assembled CORINE Land Cover Map (100 × 100 m) and the Upscaled Map With Predominantly Pure 1 × 1 km Pixels for the European Subset

Land Cover	Coverage			
	Subpixel Map		Upscaled Map	
	(km ²)	(%) ^a	(km ²)	(%) ^a
Non-irrigated arable land	715,452	26.95	439,759	16.56
Crops/wood mosaic	310,177	11.68	101,062	3.81
Pastures	239,899	9.04	81,186	3.06
Natural grassland	265,193	9.99	99,997	3.77
Mix shrubland/grassland	327,846	12.35	165,208	6.22
Broad-leaved forest	121,195	4.56	29,122	1.10
Coniferous forest	54,969	2.07	18,614	0.70
Mixed forest	127,083	4.79	41,750	1.57
Barren and sparsely vegetated areas	46,140	1.74	23,793	0.90

^aPercentage of land area pixels.

are presented in Table 2 and Figure 3. The seasonal characteristics and the phenological cycle from green-up to vegetation senescence of vegetated areas are clearly reflected by the monthly averages. From May to June, leaf emergence decreases the visible albedo and increases the near-infrared albedo, while from around July/August the vegetation senescence and increased exposure of bare ground result in the opposite spectral change. The monthly long-term mean white-sky albedo is generally higher than the mean black-sky albedo, and the difference shows an increase from May to July followed by a decrease until September.

Table 2 also includes the interannual trends of the monthly albedo averages. Simple linear trends per decade are estimated, since the interannual variation of monthly averages is not affected by a cycle pattern, such as seasonal changes. Within almost all investigated months, the visible albedo shows a negative tendency with significant trends and the near-infrared albedo shows a positive tendency with significant trends in May and September resulting in a smoothed negative tendency in the shortwave broadband. Mean negative black-sky and white-sky shortwave albedo trends of -0.0019 and -0.0034 per decade are indicated with decreasing tendencies for both albedo quantities in all months, except May. However, in contrast to the significant decreasing trends in June, July, and August, the slightly positive tendency in May is not significant. *He et al.* [2014] found that for the Northern Hemisphere from 1981 to 2010 the Global Land Surface Satellites (GLASS), Global Energy and Water Exchanges (GEWEX) project's, and International Satellite Cloud Climatology Project's (ISCCP) shortwave albedos showed similar decreasing trends in July surface albedo of -0.0013 , -0.0053 , and -0.0086 per decade, respectively. This is consistent with our results for July black-sky and white-sky shortwave albedo from the LAC AVHRR BRDF/albedo data set showing a significant decrease at a rate of -0.0039 and -0.0059 per decade, respectively, from 1990 to 2014. With a positive trend of 0.0099 per decade, the near-infrared black-sky albedo shows the strongest increase in May while in the visible broadband the negative trend is weaker than in the following months. *Zaitchik et al.* [2006] reported that positive albedo anomalies in the near-infrared broadband may reflect increased vegetation green-up in response to earlier spring warmth. May marks the end of snowmelt within the investigated subset, and the trend analysis is therefore mainly based on snow-free BRDF retrievals. Furthermore, in the first couple of years, most albedo retrievals for potentially snow covered pixels in the Alpine Region are missing due to the lower data coverage during late winter/early spring. The albedo trends for these pixels (e.g., related to changes in snow cover extent), consequently, are not included as the trend analysis is solely based on pixels with a retrieval in all years from 1990 to 2014. Thus, the positive tendency in May shortwave albedo is possibly due to an increasingly earlier start of green-up.

Table 2. Long-Term Means and Trends of Monthly AVHRR Albedo Averages in the Shortwave, Near-Infrared, and Visible Broadbands From 1990 to 2014 for Europe^a

	Monthly Average (BSA/WSA)			Trend (BSA/WSA)		
	SW	VIS	NIR	SW	VIS	NIR
May	0.178/0.197	0.056/0.062	0.303/0.335	0.0008/0.0001	$-0.0082^b/-0.0097^b$	$0.0099^b/0.0100^b$
Jun	0.176/0.200	0.052/0.060	0.303/0.343	$-0.0037^b/-0.0052^b$	$-0.0097^b/-0.0117^b$	$0.0021/0.0010$
Jul	0.168/0.191	0.055/0.063	0.285/0.323	$-0.0039^b/-0.0059^b$	$-0.0084^b/-0.0103^b$	$0.0002/-0.0021$
Aug	0.160/0.178	0.057/0.063	0.265/0.293	$-0.0022^c/-0.0043^b$	$-0.0098^b/-0.0119^b$	$0.0050^b/0.0028$
Sep	0.157/0.166	0.056/0.059	0.259/0.274	$-0.0003/-0.0014$	$-0.0086^b/-0.0096^b$	$0.0076^b/0.0065^c$

^aResults before the slash are for black-sky albedo and after the slash for white-sky albedo.

^b p value < 0.02.

^c p value < 0.05.

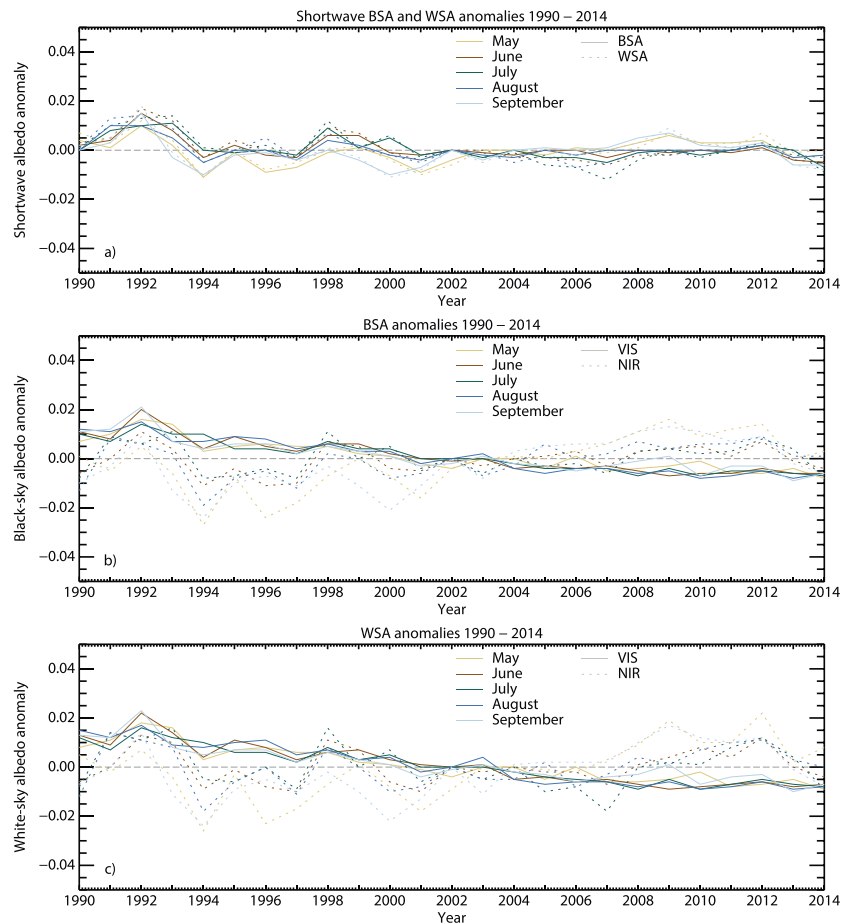


Figure 3. (a) Total shortwave black-sky and white-sky and visible and near-infrared broadband (b) black-sky and (c) white-sky albedo anomalies for Europe in May, June, July, August, and September from 1990 to 2014.

In the time series of albedo anomalies, the interannual variation is larger in the near-infrared broadband than in the visible broadband, while the total shortwave albedo anomalies clearly reveal the smallest variations (Figure 3). This implies that anomalies in the near-infrared and visible broadbands are often contrasting; and thus, through the conversion to shortwave broadband, most of the variations present in the visible and near-infrared anomalies are balanced. However, the shortwave albedo anomalies are not necessarily equal to the sum of the anomalies in the visible and near-infrared as the shortwave albedo data have their own weighting and errors. The contrast between the visible and near-infrared albedo anomalies is mainly due to the differentiated responses of vegetation to climatic variation, since, for example, the physical coupling between temperature and soil moisture may cause differing changes in the vegetation structure for most ecosystem types [Elvidge, 1990; Zhang *et al.*, 2013]. For instance, a decrease in soil moisture leads to an increase of reflectance of soils throughout all wavelengths with an enhanced spectral sensitivity at larger wavelengths [Lobell and Asner, 2002; Whiting *et al.*, 2004]. In addition, water stress may impair the normal growth of plants, and consequently, in the blue and red wavelength ranges, the absorption of radiation by chlorophyll is reduced, which results in a positive albedo anomaly in the visible band [Lillesand *et al.*, 2008]. While plant reflectance in the visible range is predominantly governed by the absorption of chlorophyll, reflectance of plants in the near-infrared broadband is most sensitive to internal structure changes (especially from 0.74 to 1.3 μm) and leaf-water variation (within the 1.3–2.5 μm range) but is also greatly influenced by plant density, plant type, and the leaf area index [Ollinger, 2011]. Hence, its variation results from a comprehensive combination of multiple factors [Jacquemoud, 1993; Ceccato *et al.*, 2001]. This contributes to the higher interannual variation of the albedo anomalies in the near-infrared broadband. Accordingly, different types of mechanisms may lead to an opposite anomaly in the near-infrared reflectance.

Under water stress, the effectiveness of the multiple scattering that usually takes place between the spongy mesophyll cells is reduced causing a decline in reflectance in the near-infrared [Elvidge, 1990; Clark, 1999; Salama, 2011]. Furthermore, leaves may alter their orientation and thereby increase the fraction of exposed bare soil. Given a plant cover with higher reflectance in the near-infrared than soil, this results in a decreased near-infrared reflectance. However, as the increase in reflectance of soils due to decreasing soil moisture is reinforced with increase in wavelength and leaves show a similar reflectance pattern regarding leaf water content, some mechanisms may as well counteract these changes in the near-infrared reflectance.

On the basis of MODIS retrievals, Teuling and Seneviratne [2008] found that during heat waves, such as in 2003 in Europe, the mechanisms resulting in a decrease of near-infrared reflectance are dominant. The negative anomalies in the near-infrared range and the contrasting positive anomalies in the visible range for 2003 can be observed in the AVHRR albedo climatology (Figure 3), especially during the peak of the heat wave in July and August. The shortwave climatology, on the other hand, shows no striking anomalies for 2003. This indicates that analysis of only total shortwave albedo variation is insufficient to correctly assess albedo anomalies related to climate variation and ecological response. Furthermore, patterns of change are spatially complex, and according to Zscheischler *et al.* [2013] not only temporal but also spatiotemporal analysis is required to capture ecological responses to climatic events.

4.2. Spatial Distribution of Annual Albedo Anomaly

The importance of spatiotemporal analysis for accurate assessment of albedo response [Zscheischler *et al.*, 2013] is considered in this section by exploring the spatial distribution of albedo anomalies over the European subset at the example of August white-sky albedo. Figure 4 displays the annual pixel-wise departure of median visible (left image) and near-infrared (right image) white-sky albedo in August from the long-term mean from 1990 to 2014. Considerable regional differences in the magnitude of the albedo anomalies are recognizable. However, in most years, the anomalies show an overall contrasting pattern over almost the entire European subset with anomalies either consistently positive in the visible and negative in the near-infrared (e.g., 1994 and 2003) or vice versa (e.g., 2011 and 2012). On the other hand, years with a mix of positive and negative anomalies within both broadbands (e.g., 2006) and years with consistently mainly positive (e.g., 1991, 1992, and 1993) or negative (e.g., 2004) albedo anomalies in the visible and near-infrared broadbands are less frequent.

The center of the heat wave in 2003 is clearly reflected by the amplitude of the albedo anomalies. Record-breaking temperatures were reached over much of western and central Europe with the areas of largest positive anomalies centered over France and Switzerland [Beniston, 2004; Schär *et al.*, 2004; Zaitchik *et al.*, 2006]. The high temperatures during and before the heat wave were associated with large precipitation deficits resulting in extremely low soil moisture across Europe. Figure 5 illustrates the spatial distribution of temperature anomalies in July and August and of precipitation anomalies in August and the preceding months (mean of the monthly anomalies from May to July). In large parts of the European subset, the precipitation anomalies in 2003 reached monthly precipitation deficits of more than 50 mm. The characteristics indicating water stress, explained in the previous section, are clearly displayed by the white-sky albedo anomalies being positive in the visible range and negative in the near-infrared range. Across most of the European subset, drought conditions resulted in positive visible albedo anomalies, with the largest positive anomalies found in France. In the Alpine region, a few large negative visible albedo anomalies can be observed which are further noticeable in the near-infrared range. These negative anomalies can very likely be attributed to increased snowmelt. The distribution of the negative near-infrared albedo anomalies generally corresponds nicely to the spatial pattern of the negative precipitation anomalies in August and the preceding months and the spatial pattern of the positive temperature anomalies. Negative near-infrared albedo anomalies dominate over large parts of the subset. However, the spatial pattern in the magnitude of the near-infrared and the magnitude of the visible albedo anomalies is somewhat different as their variation, especially in the near-infrared, results from a combination of various factors. Water stress characteristics are likewise displayed by the visible and near-infrared albedo anomalies in 1994. On the seasonal scale (June, July, and August), the major heat wave in 1994 was less pronounced, but during its culmination in July, the temperature reached anomalies of more than 4°C over Southern and Central Europe (see Figure 5) [Fischer *et al.*, 2007]. The precipitation was anomalously low in the months preceding August, except over Italy and most of France, while in August negative precipitation

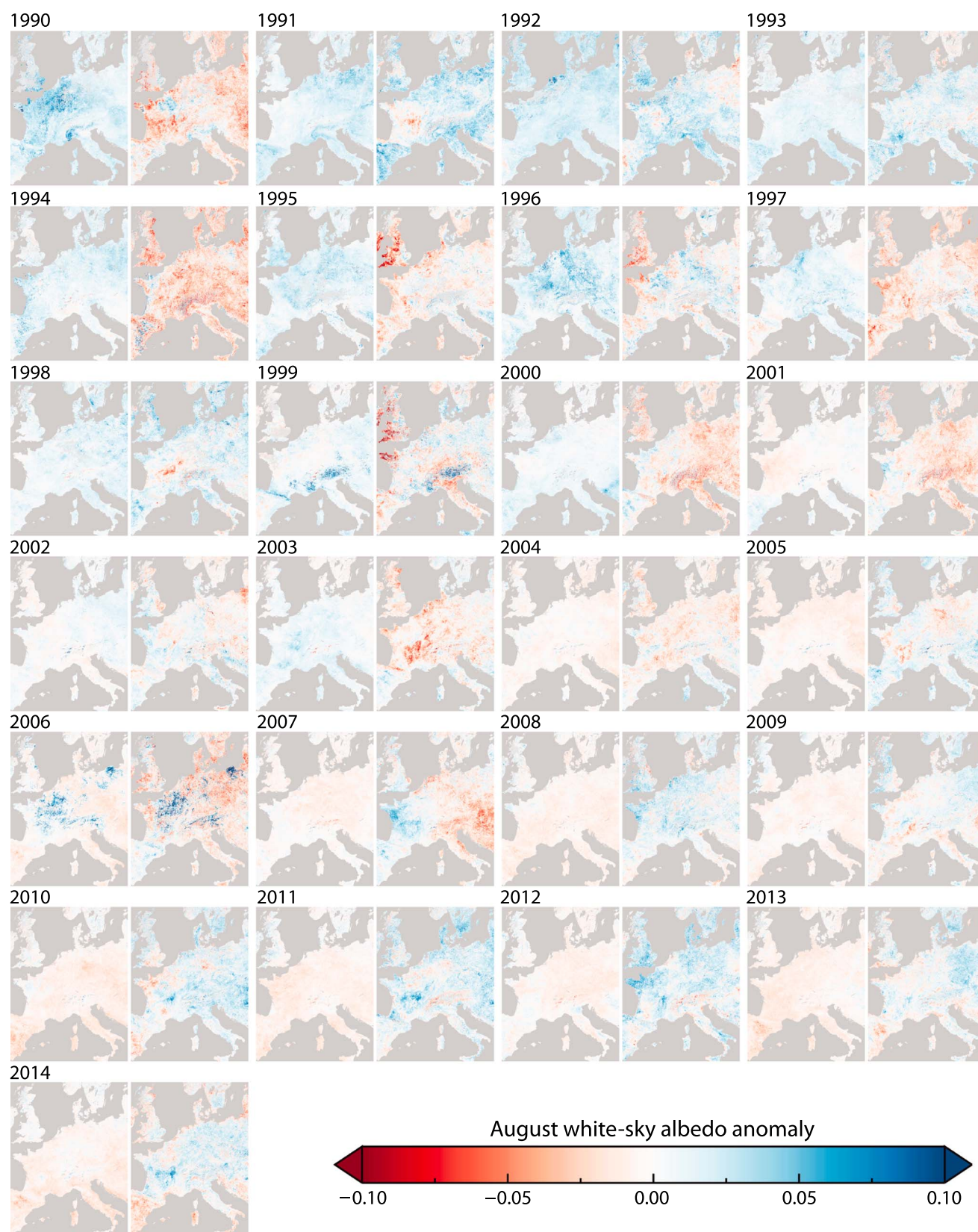


Figure 4. Spatial representation of annual August white-sky albedo anomalies over Europe from 1990 to 2014 in the visible (left images) and near-infrared (right images) broadbands.

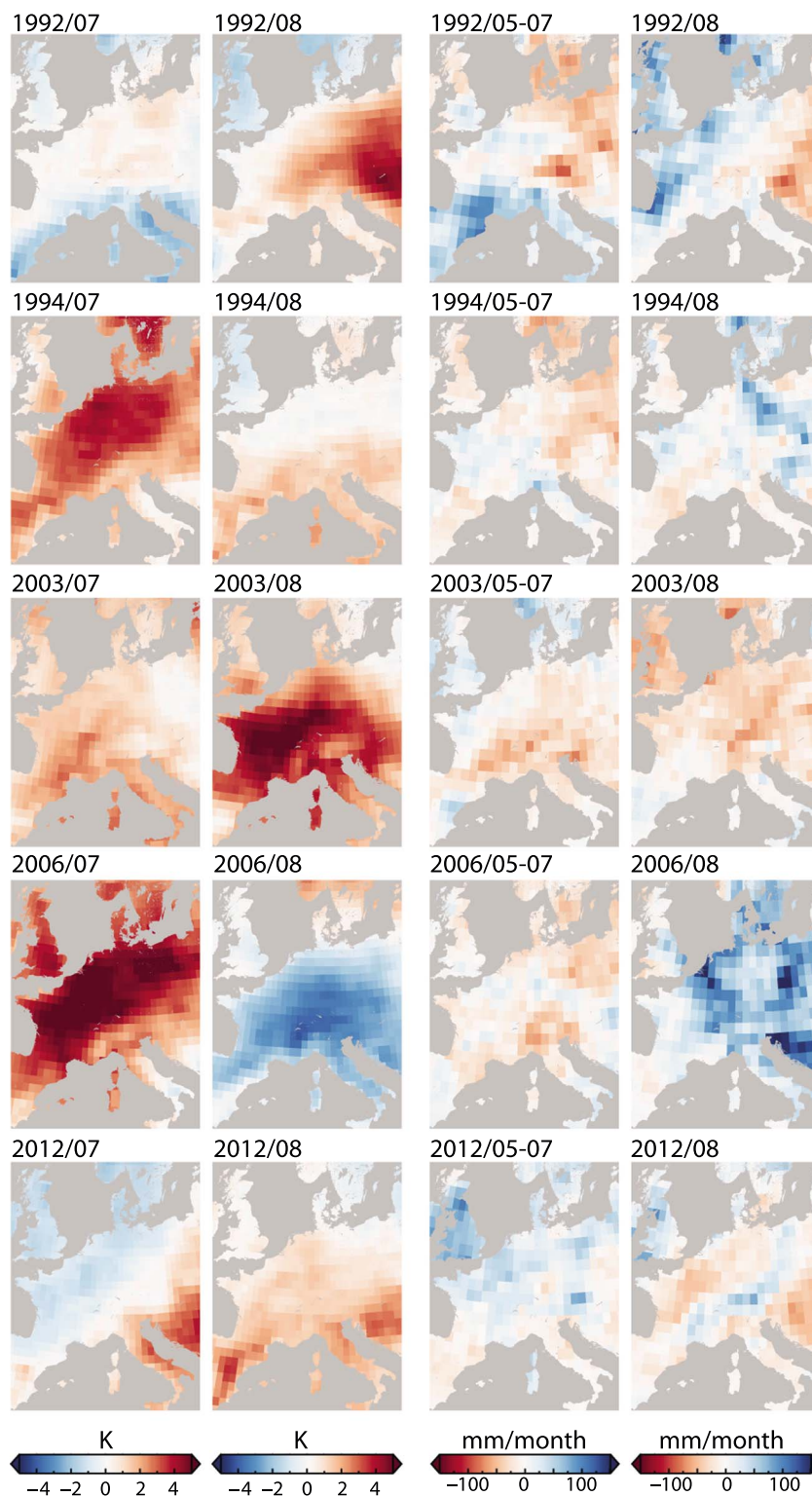


Figure 5. Climate anomalies over Europe in 1992, 1994, 2003, 2006, and 2012: temperature anomaly at 2 m for July (first column) and August (second column) and precipitation anomaly for May to July (third column) and August (fourth column). Notice the opposite color bars for temperature (blue to red) and precipitation (red to blue) anomalies.

anomalies were predominantly located in the southern part of the subset around the Mediterranean and over the United Kingdom (UK). *Fischer et al.* [2007], for example, found that local drying, which was strongest in June and July, led to extremely limited evaporation and large numbers of hot days around the Mediterranean in August. The opposite white-sky albedo anomalies in August 1994 are accordingly less pronounced in the amplitude compared to 2003, but the area with contrasting anomalies in the visible and near-infrared broadband is extensive due to the widespread drought and evenly covers most of the European subset, including the Mediterranean Region. Compared to 1994 and 2003 when precipitation deficits coupled with high temperatures triggered an extreme response of vegetation, in 2011 and 2012 the high temperatures in August were associated with positive precipitation anomalies in the preceding months and spatially variable and rather weak anomalies in August. Figure 5 illustrates the climate anomalies for 2012. These conditions led to positive anomalies in the Fraction of Absorbed Photosynthetically Active Radiation (FAPAR) in Europe [Blunden and Arndt, 2012, 2013]. Thus, for these years the surface albedo shows mainly negative anomalies in the visible range and positive anomalies in the near-infrared range.

Starting in 1991, positive albedo anomalies in both broadbands are displayed almost throughout the entire European subset for three successive years (Figure 4). Several studies reported impacts of volcanic aerosol on the global climate of these years related to the eruption of Mount Pinatubo in the Philippines in June 1991. In accordance with the displayed positive visible and near-infrared broadband albedo anomalies, *Riihelä et al.* [2013] identified positive shortwave black-sky albedo anomalies between mid-1990 and 1994 at midlatitudes in CM SAF cLOUD, Albedo and Radiation from coarse resolution AVHRR (Global Area Coverage) data 1st Release-Surface Albedo (CLARA-A1-SAL) and found that these features correlate with an increase in midlatitude Aerosol Optical Depth observed in the Total Ozone Mapping Spectrometer aerosol time series [Torres et al., 2002]. Following the eruption, stratospheric aerosol showed a peak of global visible optical depth of 0.15 [Hansen et al., 1992; Minnis et al., 1993], and by spring 1992, the volcanic aerosol cloud had extended into both hemispheres. This resulted in an increase in reflection of up to an additional 2.5 W/m^2 solar radiation over the two years following the eruption [Wielicki et al., 2005; Harries and Futyran, 2006]. The radiative effects of the stratospheric veil of aerosol substantially affected the subsequent temperature (e.g., a cooling signature, especially, in the second and third summer following the tropical eruptions) [Free and Angell, 2002; Jones et al., 2004] and precipitation [Trenberth and Dai, 2007] and consequently influenced the reflectance properties of the surface.

Positive albedo anomalies in both broadbands on a more regional scale are also displayed in the surface albedo retrievals for 2006, but the anomalies are more pronounced and strikingly higher. These regional positive albedo anomalies coincide with regions that experienced heavy rainfall in August 2006 (Figure 5). In large parts of northern France, Germany, Poland, and northern of the Adriatic Sea, August precipitation anomalies amounted to more than 140 mm. High precipitation events are usually accompanied by overcast sky conditions, which pose considerable problems for the retrieval of surface albedo [Sütterlin et al., 2015]. Therefore, in this case, the strikingly high positive albedo anomalies are potentially artifacts caused by haze and residual clouds in the subpixel scale of pixels improperly indicated as cloud-free.

Overall, the albedo anomalies nicely reflect the spatial pattern in climate variation, but additional regional differences in responsiveness can be observed, which are likely related to the predominant land cover type. The relationship between interannual albedo variation and different land cover types is explored in the next section.

4.3. Land Cover-Dependent Intraseasonal and Interannual Variations of Albedo

The intraseasonal white-sky albedo anomaly is decomposed into land cover-dependent visible and near-infrared broadband white-sky albedo anomalies for pastures, natural grasslands, non-irrigated arable lands, broad-leaved forests, and coniferous forests at the example of the 2003 heat wave in Figure 6. With the beginning of the heat wave around June/July, positive visible and negative near-infrared albedo anomalies can be observed due to the vegetation's response to water stress as explained in the previous section. Among the different land cover types, considerable differences in the magnitude and timeliness of the albedo anomalies are recognizable while the grasses and non-irrigated arable lands albedo anomalies are mostly more pronounced and instantaneous than the forest group anomalies. This is consistent with the differing vegetation response of these land cover types as, for example, grasses are generally more susceptible to water stress and lose biomass more quickly in drought conditions than trees, but are also the first to recover [van Wijk and Rodriguez-Iturbe, 2002; Xu et al., 2015].

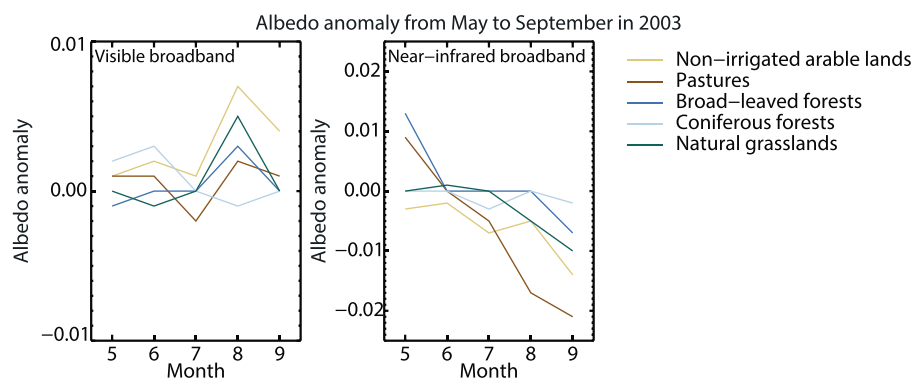


Figure 6. Visible and near-infrared broadband white-sky albedo anomalies of non-irrigated arable lands, pastures, broad-leaved forests, coniferous forests, and natural grasslands from May to September during the 2003 heat wave.

Land surface albedo and the climate-driven albedo response of any geographic region accordingly vary depending on the predominant type of land cover and the density and structure of that land cover. Therefore, it is of interest to investigate the interannual and intraseasonal variations of albedo for the various land cover types of the heterogeneous European land surface. Figure 7 shows the long-term mean and the interannual standard deviation (SD) of monthly shortwave, visible, and near-infrared white-sky albedo averages from 1990 to 2014 for nine typical types of vegetation cover for the months from approximately green-up to vegetation senescence. Two standard deviations from the mean are illustrated, except for the mean of barren and sparsely vegetated areas in May and June with ± 1 time the standard deviation. For vegetated areas, the variation of the albedo for these 5 months displays a typical phenology, where plant growth increases (decreases) the near-infrared (visible) broadband albedo, and vegetation senescence decreases (increases) the albedo in the near-infrared (visible) broadband. Thereby, the phenological pattern in the visible range is quite similar for all vegetated land cover types, while in the near-infrared the pattern differs among the vegetated areas and is generally higher. In contrast, barren and sparsely vegetated areas show different features, because these areas are predominantly located at higher altitudes and are consequently mostly affected by snow. As snow adds to the albedo throughout all wavelengths, the albedo of these areas is highest in May for all broadbands and sharply decreases until July. Accordingly, the barren and sparsely vegetated areas show the highest intraseasonal variation ($SD_{SW} = 0.066$, $SD_{VIS} = 0.066$, and $SD_{NIR} = 0.069$), followed by non-irrigated arable lands ($SD_{SW} = 0.021$, $SD_{VIS} = 0.005$, and $SD_{NIR} = 0.046$). Contrarily, the smallest intraseasonal variation is found for coniferous forests ($SD_{SW} = 0.008$ and $SD_{NIR} = 0.016$) and mix shrublands/grasslands ($SD_{SW} = 0.006$, $SD_{NIR} = 0.01$) in the shortwave and near-infrared ranges and for pastures ($SD_{VIS} = 0.002$) in the visible range, respectively.

The monthly interannual standard deviations indicate the smallest variation for total shortwave albedo, with values of less than 0.01 in all 5 months, except for barren and sparsely vegetated areas. This is consistent with findings based on MODIS observations from four consecutive years (2001–2003) by Gao *et al.* [2005] reporting that interannual differences between minimum and maximum snow-free shortwave white-sky albedos are mostly less than 0.01. In the visible and near-infrared ranges, the monthly interannual standard deviations show an opposite pattern during the investigated months for most of the land cover types. The SD in the near-infrared range is high in May, decreases during the growing season, and increases during vegetation senescence, while the generally lower SD in the visible range roughly increases during the growing season and decreases during vegetation senescence. Exceptionally high interannual SDs are found for barren and sparsely vegetated areas from May to July and are presumably related to the variation in snowmelting dates between different years. The next highest interannual variation for these months is observed for natural grasslands and forests in the shortwave and near-infrared ranges, respectively, for broad-leaved forests, non-irrigated arable lands, and crops in the visible broadband. Crops also show the highest interannual variation in the visible range for the later months, while pastures in particular display the highest interannual near-infrared and shortwave albedo variation. Cultivation change, crop rotation, and fallow years most likely add to the high variability in albedo for crops and non-irrigated arable lands, especially in the visible range. Grasslands show a large variability with respect to the diversity of grasses, leaf area, dead material, gap frequency, and underlying

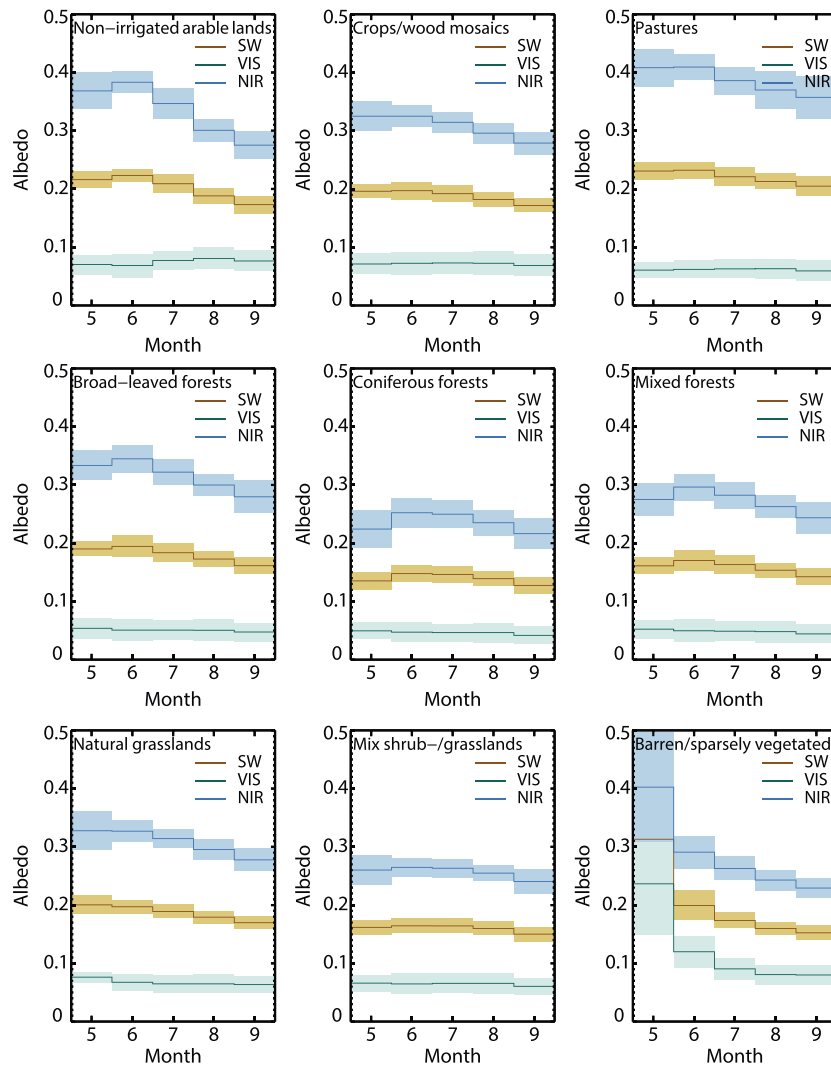


Figure 7. Long-term mean of monthly white-sky albedo averages from May to September ± 2 times the interannual standard deviation for different land cover types, except for May and June albedo of barren and sparsely vegetated areas with ± 1 time the interannual standard deviation.

soil types. Therefore, their high interannual albedo variation, mainly in the near-infrared, may be related to the quick response of these features to interannual changes in climate parameters, for example, regarding to soil moisture. Apart from the interannual SD in the albedo of barren and sparsely vegetated areas, the SDs in visible, near-infrared, and shortwave albedos for the different land cover types are lower than 0.015, which is similar to those observed by Fang *et al.* [2007]. However, the land cover types that show higher and lower interannual variations are different for the three broadbands. This indicates differences among the land cover types regarding the sensitivity of vegetation response in the visible and near-infrared ranges.

5. Conclusions

In this work, the first 25 year data set (1990 to 2014) of AVHRR BRDF/albedo retrievals with 1 km resolution is presented and examined for the months from approximately green-up to vegetation senescence (May to September) in Europe. Spatiotemporal patterns and intraseasonal and interannual variations of albedo for different land cover types were assessed by utilizing spatial monthly albedo averages and monthly albedo anomalies derived from BRDF/albedo retrievals in the visible, near-infrared, and total shortwave broadbands. Intraseasonally, the monthly albedo averages displayed the typical characteristics from vegetation emergence (decrease in visible and increase

in near-infrared albedo) to senescence (increase in visible and decrease in near-infrared albedo). Monthly visible and near-infrared albedo averages were found to depart in opposite ways from the long-term mean in most years. This can mainly be attributed to the contrasting response of visible and near-infrared albedos to climate-driven anomalous soil moisture conditions. On the basis of contrasting MODIS albedo anomalies during the 2003 European heat wave, *Teuling and Seneviratne* [2008] pointed out that in order to capture the response of albedo to variation in soil moisture, not only the direct effect of soil moisture on albedo but also the spectrally complex and differing response of vegetation to water stress should be taken into account. Our investigation of the AVHRR albedo anomalies supports this finding and expands its scope to nonheat wave years and years without water stress, such as years with positive precipitation anomalies. Although the anomalies in the total shortwave albedo are not necessarily equal to the sum of these contrasting anomalies in the visible and near-infrared broadbands, most of the variation in the visible and near-infrared albedo anomalies is averaged through the conversion to shortwave. Accordingly, in the shortwave albedo climatology, the years associated with striking climate events, such as heat waves or conditions leading to pronounced anomalies in the Fraction of Absorbed Photosynthetically Active Radiation (FAPAR), showed only diminished or no striking monthly anomalies. Thus, in order to adequately capture the responses of albedo to climate events, the investigation of shortwave albedo is insufficient as the differing variation between spectral albedos is crucial.

Furthermore, the correct assessment of albedo anomalies related to climate variation requires spatial analysis. The spatial distribution illustrated at the example of August white-sky albedo indicated that years with a widespread pattern of almost consistently positive or negative albedo anomalies in the visible range and contrasting anomalies in the near-infrared range throughout the European subset are the most common and clearly revealed regional differences in the magnitude of the pixel-wise albedo anomalies. Responses to climatic events, such as the heat wave in 2003, become apparent and the center of the events is depicted in the amplitude of the spatial albedo anomalies. In contrast to years with severe drought, years with conditions that are favorable for the vegetation resulted in generally negative visible and positive near-infrared albedo anomalies. Overall, the spatial distribution in climate variation is appropriately reflected in the albedo anomalies from 1990 to 2014. Yet although the AVHRR BRDF/albedo data are cloud cleared and atmospherically corrected, residual cloud contamination that may sometimes occur in magnitude (backup) retrievals can still affect albedo retrievals.

The AVHRR albedos further capture regional patterns introduced by differences in the effects of climate variation for different land cover types. Except for the barren and sparsely vegetated areas, the different types of land cover showed interannual standard deviations lower than 0.015 in all broadbands, while with values less than 0.01 the variation is smallest in the shortwave broadband. Barren and sparsely vegetated areas generally presented the highest interannual standard deviation in May, June, and July albedo. In the shortwave and near-infrared ranges, natural grassland and forest albedos and in the visible broadband, broad-leaved forest, non-irrigated arable land, and crop albedos showed the next highest interannual standard deviation for these months. Crops also displayed the highest interannual visible albedo variation for the later months (July to September), while in the near-infrared broadband and in the shortwave broadband the highest variation was found for the albedo of pastures. Thus, the land cover types with higher and lower interannual variations were found to differ between the broadbands as well as intraseasonally. Accordingly, differences in the responsiveness of land cover types between the visible and near-infrared broadband are revealed. Such findings and the comprehensive view in terms of temporal extent are essential for climate modelers in order to improve the characterization of land cover albedo. Further, the spectrally complex dynamics of albedo in response to climate variation indicate the decisive role of soil moisture and demonstrate the importance of differentiating between spectral albedo responses and to take contributions from soil and vegetation into account when representing albedo in climate modeling.

In summary, the AVHRR BRDF/albedo climatology for the months from May to September was found to capture temporal and spatial patterns that are appropriate for the prevailing land cover type and to accurately reflect the associated climate variation. This confirms the data set's potential to contribute to more adequate representation of surface albedo in climate models. The presented spatial and temporal albedo variations also imply the need for more detailed spatiotemporal investigation of albedo for other seasons. Future work could, for example, focus on the months with snow conditions, which in combination with complex terrains pose considerable problems for the retrieval of surface albedo. It is further recommended to focus on the important role of soil moisture in shaping albedo variation and account for both the effects of moisture on soil albedo and the complex albedo response of vegetation.

Acknowledgments

This study was funded by the Swiss National Science Foundation (SNSF) (project 200020 132172). The authors acknowledge the Global Precipitation Climatology Centre (GPCC) operated by the German National Meteorological Service for providing precipitation monitoring data (ftp://ftp.dwd.de/pub/data/gpcc/monitoring_v5) and the European Center for Medium-range Weather Forecasting (ECMWF) for providing ERA-Interim Reanalysis data (<http://apps.ecmwf.int/datasets>). Coordinate Information on the Environment (CORINE) Land cover Classification (CLC) data (www.eea.europa.eu/data-and-maps/data) was acquired from the European Environmental Agency (EEA). The authors gratefully acknowledge the MODIS Research group of the Center for Remote Sensing at the Boston University and the School for the Environment at the University of Massachusetts Boston and support from NASA grant NNX12AL38G. Special thanks go to Jan Musial (jan.musial@igik.edu.pl) for his work on the Probabilistic Cloud Masks (PCM), to Fabia Hüslér (fabia.huesler@giub.unibe.ch) for her work on the snow masks, and to Christoph Neuhaus for his valuable inputs on the data processing.

References

- Beniston, M. (2004), The 2003 heat wave in Europe: A shape of things to come? An analysis based on Swiss climatological data and model simulations, *Geophys. Res. Lett.*, *31*, L02202, doi:10.1029/2003GL018857.
- Blunden, J., and D. S. Arndt (2012), State of the climate in 2011, *Bull. Am. Meteorol. Soc.*, *93*(7), S1–S282, doi:10.1175/2012BAMSStateoftheClimate.1.
- Blunden, J., and D. S. Arndt (2013), State of the climate in 2012, *Bull. Am. Meteorol. Soc.*, *94*(8), S1–S258, doi:10.1175/2013BAMSStateoftheClimate.1.
- Boisier, J. P., N. de Noblet-Ducoudré, and P. Ciais (2013), Inferring past land use-induced changes in surface albedo from satellite observations: A useful tool to evaluate model simulations, *Biogeosciences*, *10*(3), 1501–1516, doi:10.5194/bg-10-1501-2013.
- Ceccato, P., S. Flasse, S. Tarantola, S. Jacquemoud, and J.-M. Grégoire (2001), Detecting vegetation leaf water content using reflectance in the optical domain, *Remote Sens. Environ.*, *77*(1), 22–33, doi:10.1016/S0034-4257(01)00191-2.
- Clark, R. N. (1999), Spectroscopy of rocks and minerals, and principles of spectroscopy, in *Manual of Remote Sensing, Remote Sensing for the Earth Sciences*, vol. 3, edited by A. N. Rencz, pp. 3–58, John Wiley, New York.
- Dee, D. P., et al. (2011), The ERA-Interim reanalysis: Configuration and performance of the data assimilation system, *Q. J. R. Meteorol. Soc.*, *137*(656), 553–597, doi:10.1002/qj.828.
- Elvidge, C. D. (1990), Visible and near infrared reflectance characteristics of dry plant materials, *Int. J. Remote Sens.*, *11*(10), 1775–1795, doi:10.1080/01431169008955129.
- Fang, H., S. Liang, H.-Y. Kim, J. R. Townshend, C. B. Schaaf, A. H. Strahler, and R. E. Dickinson (2007), Developing a spatially continuous 1 km surface albedo data set over North America from Terra MODIS products, *J. Geophys. Res.*, *112*, D20206, doi:10.1029/2006JD008377.
- Fischer, E. M., S. I. Seneviratne, D. Lüthi, and C. Schär (2007), Contribution of land-atmosphere coupling to recent European summer heat waves, *Geophys. Res. Lett.*, *34*, L06707, doi:10.1029/2006GL029068.
- Free, M., and J. K. Angell (2002), Effect of volcanoes on the vertical temperature profile in radiosonde data, *J. Geophys. Res.*, *107*(D10), 4101, doi:10.1029/2001JD001128.
- Gao, F., C. B. Schaaf, A. H. Strahler, A. Roesch, W. Lucht, and R. Dickinson (2005), MODIS bidirectional reflectance distribution function and albedo Climate Modeling Grid products and the variability of albedo for major global vegetation types, *J. Geophys. Res.*, *110*, D01104, doi:10.1029/2004JD005190.
- Global Climate Observing System (2004), GCOS—92, Implementation Plan for the Global Observing System for Climate in Support of the UNFCCC.
- Global Climate Observing System (2011), Global Climate Observing System GCOS-154, systematic observation requirements for satellite-based products for climate, 2011: Update, supplemental details to the satellite-based component of the "Implementation Plan for the Global Observing System for Climate in Support of the UNFCCC" 2010 update, December 2011.
- Hansen, J., A. Lacis, R. Ruedy, and M. Sato (1992), Potential climate impact of Mount Pinatubo eruption, *Geophys. Res. Lett.*, *19*(2), 215–218, doi:10.1029/91GL02788.
- Harries, J. E., and J. M. Fyfe (2006), On the stability of the Earth's radiative energy balance: Response to the Mt. Pinatubo eruption, *Geophys. Res. Lett.*, *33*, L23814, doi:10.1029/2006GL027457.
- He, T., S. Liang, and D.-X. Song (2014), Analysis of global land surface albedo climatology and spatial-temporal variation during 1981–2010 from multiple satellite products, *J. Geophys. Res. Atmos.*, *119*, 10,281–10,298, doi:10.1002/2014JD021667.
- Heidinger, A. K., W. C. Straka, C. C. Molling, J. T. Sullivan, and X. Wu (2010), Deriving an inter-sensor consistent calibration for the AVHRR solar reflectance data record, *Int. J. Remote Sens.*, *31*(24), 6493–6517, doi:10.1080/01431161.2010.496472.
- Heymann, Y., C. Steenmans, G. Croisille, and M. Bossard (1994), *CORINE Land Cover. Technical Guide*, Office for Official Publications of the European Communities, Luxembourg.
- Hüslér, F., F. Fontana, C. Neuhaus, M. Riffler, J. Musial, and S. Wunderle (2011), AVHRR archive and processing facility at the University of Bern: A comprehensive 1-km satellite data set for climate change studies, *EARSeL EProc.*, *10*(2), 83–101.
- Jacquemoud, S. (1993), Airborne Imaging Spectrometry Inversion of the PROSPECT + SAIL canopy reflectance model from AVIRIS equivalent spectra: Theoretical study, *Remote Sens. Environ.*, *44*(2), 281–292, doi:10.1016/0034-4257(93)90022-P.
- Jin, Y., C. B. Schaaf, F. Gao, X. Li, A. H. Strahler, W. Lucht, and S. Liang (2003), Consistency of MODIS surface bidirectional reflectance distribution function and albedo retrievals: 1. Algorithm performance, *J. Geophys. Res.*, *108*(D5), 4158, doi:10.1029/2002JD002803.
- Jones, P. D., A. Moberg, T. J. Osborn, and K. R. Briffa (2004), Surface climate responses to explosive volcanic eruptions seen in long European temperature records and mid-to-high latitude tree-ring density around the Northern Hemisphere, in *Volcanism and the Earth's Atmosphere*, edited by A. Robock and C. Oppenheimer, pp. 239–254, AGU, Washington, D. C.
- Lawrence, P. J., and T. N. Chase (2007), Representing a new MODIS consistent land surface in the Community Land Model (CLM 3.0), *J. Geophys. Res.*, *112*, G01023, doi:10.1029/2006JG000168.
- Lewis, P., and M. J. Barnsley (1994), Influence of the sky radiance distribution on various formulations of the Earth surface albedo, in *Proceedings of the Colloque International Mesures Physiques et Signatures en Teledetection*, pp. 707–716, Val d'Isère, France.
- Li, Z., and L. Garand (1994), Estimation of surface albedo from space: A parameterization for global application, *J. Geophys. Res.*, *99*(D4), 8335–8350, doi:10.1029/94JD00225.
- Lillesand, T. M., R. W. Kiefer, and J. Chipman (2008), Concepts and foundations of remote sensing, in *Remote sensing and Image Interpretation*, pp. 1–60, John Wiley, New York.
- Liu, J., C. B. Schaaf, A. H. Strahler, Z. Jiao, Y. Shuai, Q. Zhang, M. Roman, J. A. Augustine, and E. G. Dutton (2009), Validation of Moderate Resolution Imaging Spectroradiometer (MODIS) albedo retrieval algorithm: Dependence of albedo on solar zenith angle, *J. Geophys. Res.*, *114*, D01106, doi:10.1029/2008JD009969.
- Lobell, D. B., and G. P. Asner (2002), Moisture effects on soil reflectance, *Soil Sci. Soc. Am. J.*, *66*(3), 722–727, doi:10.2136/sssaj2002.7220.
- Loew, A., P. M. van Bodegom, J.-L. Widłowski, J. Otto, T. Quaipe, B. Pinty, and T. Raddatz (2014), Do we (need to) care about canopy radiation schemes in DGVMs? Caveats and potential impacts, *Biogeosciences*, *11*(7), 1873–1897, doi:10.5194/bg-11-1873-2014.
- Lucht, W., C. B. Schaaf, and A. H. Strahler (2000), An algorithm for the retrieval of albedo from space using semiempirical BRDF models, *IEEE Trans. Geosci. Remote Sens.*, *38*(2), 977–998, doi:10.1109/36.841980.
- Minnis, P., E. F. Harrison, L. L. Stowe, G. G. Gibson, F. M. Denn, D. R. Doelling, and W. L. Smith (1993), Radiative climate forcing by the Mount Pinatubo eruption, *Science*, *259*(5100), 1411–1415, doi:10.1126/science.259.5100.1411.
- Nicodemus, F. E., J. C. Richmond, J. J. Hsia, I. W. Ginsberg, and T. Limperis (1977), *Geometrical Considerations and Nomenclature for Reflectance*, U.S. Dept. of Commerce, National Bureau of Standards, Washington.
- Ollinger, S. V. (2011), Sources of variability in canopy reflectance and the convergent properties of plants, *New Phytol.*, *189*(2), 375–394, doi:10.1111/j.1469-8137.2010.03536.x.

- Pineda, N., O. Jorba, J. Jorge, and J. M. Baldasano (2004), Using NOAA AVHRR and SPOT VGT data to estimate surface parameters: Application to a mesoscale meteorological model, *Int. J. Remote Sens.*, 25(1), 129–143, doi:10.1080/0143116031000115201.
- Pinty, B., T. Laverigne, T. Kaminski, O. Aussedat, R. Giering, N. Gobron, M. Taberner, M. M. Verstraete, M. Voßbeck, and J.-L. Widlowski (2008), Partitioning the solar radiant fluxes in forest canopies in the presence of snow, *J. Geophys. Res.*, 113, D04104, doi:10.1029/2007JD009096.
- Pitman, A. J. (2003), The evolution of, and revolution in, land surface schemes designed for climate models, *Int. J. Climatol.*, 23(5), 479–510, doi:10.1002/joc.893.
- Price, J. C. (1991), Timing of NOAA afternoon passes, *Int. J. Remote Sens.*, 12(1), 193–198, doi:10.1080/01431169108929644.
- Rao, C. R. (1987), Pre-launch calibration of channels 1 and 2 of advanced very high resolution radiometer, NOAA technical report NESDIS 36, NOAA Tech. Rep. NESDIS 36, Dept. of Commerce.
- Riihela, A., T. Manninen, V. Laine, K. Andersson, and F. Kaspar (2013), CLARA-SAL: A global 28 yr time series of Earth's black-sky surface albedo, *Atmos. Chem. Phys.*, 13(7), 3743–3762, doi:10.5194/acp-13-3743-2013.
- Roesch, A., C. B. Schaaf, and F. Gao (2004), Use of Moderate-Resolution Imaging Spectroradiometer bidirectional reflectance distribution function products to enhance simulated surface albedos, *J. Geophys. Res.*, 109, D12105, doi:10.1029/2004JD004552.
- Román, M. O., C. B. Schaaf, P. Lewis, F. Gao, G. P. Anderson, J. L. Privette, A. H. Strahler, C. E. Woodcock, and M. Barnsley (2010), Assessing the coupling between surface albedo derived from MODIS and the fraction of diffuse skylight over spatially-characterized landscapes, *Remote Sens. Environ.*, 114(4), 738–760, doi:10.1016/j.rse.2009.11.014.
- Rudolf, B., and U. Schneider (2005), Calculation of gridded precipitation data for the global land-surface using in-situ gauge observations, in *Proceedings of the 2nd Workshop of the International Precipitation Working Group IPWG, Monterey October 2004*, pp. 231–247, Monterey.
- Salama, R. B. (2011), Remote sensing of soils and plants imagery, in *Encyclopedia of Agrophysics*, edited by J. Gliński, J. Horabik, and J. Lipiec, pp. 681–692, Springer, Dordrecht, Netherlands.
- Salomon, J. G., C. B. Schaaf, A. H. Strahler, F. Gao, and Y. Jin (2006), Validation of the MODIS bidirectional reflectance distribution function and albedo retrievals using combined observations from the Aqua and Terra platforms, *IEEE Trans. Geosci. Remote Sens.*, 44(6), 1555–1565, doi:10.1109/TGRS.2006.871564.
- Schaaf, C. B., et al. (2002), First operational BRDF, albedo nadir reflectance products from MODIS, *Remote Sens. Environ.*, 83(1–2), 135–148, doi:10.1016/S0034-4257(02)00091-3.
- Schaaf, C. B., J. Cihlar, A. Belward, E. Dutton, and M. Verstraete (2009), Albedo and reflectance anisotropy, ECV-T8, in *GTOS Assessment of the Status of the Development of Standards for the Terrestrial Essential Climate Variables*, edited by R. Sessa, FAO, Rome.
- Schaaf, C. B., J. Liu, F. Gao, and A. H. Strahler (2011), MODIS albedo and reflectance anisotropy products from Aqua and Terra, in *Land Remote Sensing and Global Environmental Change: NASA's Earth Observing System and the Science of ASTER and MODIS*, *Remote Sens. Digital Image Process. Ser.*, vol. 11, edited by B. Ramachandran, C. Justice, and M. Abrams, 873 pp., Springer.
- Schär, C., P. L. Vidale, D. Lüthi, C. Frei, C. Häberli, M. A. Liniger, and C. Appenzeller (2004), The role of increasing temperature variability in European summer heatwaves, *Nature*, 427(6972), 332–336, doi:10.1038/nature02300.
- Sütterlin, M., C. B. Schaaf, R. Stöckli, Q. Sun, F. Hüsler, C. Neuhaus, and S. Wunderle (2015), Albedo and reflectance anisotropy retrieval from AVHRR operated onboard NOAA and MetOp satellites: Algorithm performance and accuracy assessment for Europe, *Remote Sens. Environ.*, 168, 163–176, doi:10.1016/j.rse.2015.06.023.
- Teuling, A. J., and S. I. Seneviratne (2008), Contrasting spectral changes limit albedo impact on land-atmosphere coupling during the 2003 European heat wave, *Geophys. Res. Lett.*, 35, L03401, doi:10.1029/2007GL032778.
- Torres, O., P. K. Bhartia, J. R. Herman, A. Sinyuk, P. Ginoux, and B. Holben (2002), A long-term record of aerosol optical depth from TOMS observations and comparison to AERONET measurements, *J. Atmos. Sci.*, 59(3), 398–413, doi:10.1175/1520-0469(2002)059<0398:ALTR0A>2.0.CO;2.
- Trenberth, K. E., and A. Dai (2007), Effects of Mount Pinatubo volcanic eruption on the hydrological cycle as an analog of geoengineering, *Geophys. Res. Lett.*, 34, L15702, doi:10.1029/2007GL030524.
- van Wijk, M. T., and I. Rodriguez-Iturbe (2002), Tree-grass competition in space and time: Insights from a simple cellular automata model based on ecohydrological dynamics, *Water Resour. Res.*, 38(9), 1179, doi:10.1029/2001WR000768.
- Wang, K., S. Liang, C. B. Schaaf, and A. H. Strahler (2010), Evaluation of Moderate Resolution Imaging Spectroradiometer land surface visible and shortwave albedo products at FLUXNET sites, *J. Geophys. Res.*, 115, D17107, doi:10.1029/2009JD013101.
- Wang, S., A. P. Trishchenko, K. V. Khlopenkov, and A. Davidson (2006), Comparison of International Panel on Climate Change Fourth Assessment Report climate model simulations of surface albedo with satellite products over northern latitudes, *J. Geophys. Res.*, 111, D21108, doi:10.1029/2005JD006728.
- Wanner, W., X. Li, and A. H. Strahler (1995), On the derivation of kernels for kernel-driven models of bidirectional reflectance, *J. Geophys. Res.*, 100(D10), 21,077–21,089, doi:10.1029/95JD02371.
- Whiting, M. L., L. Li, and S. L. Ustin (2004), Predicting water content using Gaussian model on soil spectra, *Remote Sens. Environ.*, 89(4), 535–552, doi:10.1016/j.rse.2003.11.009.
- Widlowski, J.-L., et al. (2011), RAMI4PILPS: An intercomparison of formulations for the partitioning of solar radiation in land surface models, *J. Geophys. Res.*, 116, G02019, doi:10.1029/2010JG001511.
- Wielicki, B. A., T. Wong, N. Loeb, P. Minnis, K. Priestley, and R. Kandel (2005), Changes in Earth's albedo measured by satellite, *Science*, 308(5723), 825–825, doi:10.1126/science.1106484.
- Xu, X., D. Medvigy, and I. Rodriguez-Iturbe (2015), Relation between rainfall intensity and savanna tree abundance explained by water use strategies, *Proc. Natl. Acad. Sci. U. S. A.*, 112(42), 12,992–12,996, doi:10.1073/pnas.1517382112.
- Zaitchik, B. F., A. K. Macalady, L. R. Bonneau, and R. B. Smith (2006), Europe's 2003 heat wave: A satellite view of impacts and land-atmosphere feedbacks, *Int. J. Climatol.*, 26(6), 743–769, doi:10.1002/joc.1280.
- Zhang, N., Y. Hong, Q. Qin, and L. Liu (2013), VSDI: A visible and shortwave infrared drought index for monitoring soil and vegetation moisture based on optical remote sensing, *Int. J. Remote Sens.*, 34(13), 4585–4609, doi:10.1080/01431161.2013.779046.
- Zhang, X., S. Liang, K. Wang, L. Li, and S. Gui (2010), Analysis of global land surface shortwave broadband albedo from multiple data sources, *IEEE J. Sel. Top. Appl. Earth Obs. Remote Sens.*, 3(3), 296–305, doi:10.1109/JSTARS.2010.2049342.
- Zscheischler, J., M. D. Mahecha, S. Harmeling, and M. Reichstein (2013), Detection and attribution of large spatiotemporal extreme events in Earth observation data, *Ecol. Inf.*, 15, 66–73, doi:10.1016/j.ecoinf.2013.03.004.